Electronic Supplementary Material (ESI) for Physical Chemistry Chemical Physics
This journal is © The Owner Societies 2013

# Near-field spatial mapping of strongly interacting multiple plasmonic infrared antennas: Electronic supplemental information

Sarah E. Grefe,[1] Daan Leiva,[1] Stefan Mastel,[2] Scott D. Dhuey,[3] Stefano Cabrini,[3] P. James Schuck,[3] and Yohannes Abate[1,*]

[1] *Department of Physics and Astronomy, California State University Long Beach, Long Beach, California 90840, USA*
[2] *CIC NanoGUNE Consolider, Tolosa Hiribidea 76, 20018 Donostia San Sebastián, Spain*
[3] *The Molecular Foundry, Lawrence Berkeley National Laboratory, Berkeley, California 94720, USA*

(Dated: July 22, 2013)

We image using a cross-polarization scattering-type scanning near-field optical microscope (s-SNOM) to explore the strong coupling by exciting the antenna structures along the in-plane (sample plane), and detecting the out-of-plane near-field component, called S/P scheme (S-excitation, P-detection). Previous reported studies explored s-SNOM cross-polarization imaging of plasmonic interactions in metal nanoparticle dimers.[1–3] When imaging nanoparticles near plasmon resonances, using S/P schemes minimizes the tip-induced perturbation since the local scattered field is dominated by the localized surface plasmons and not by the incident laser's far field.[1,2] This is because the scattered field ($E_s$) is proportional to:

$$E_s \propto (1 + r_f)^2 \alpha_{eff} E_0 \propto s e^{i\alpha} E_0 \tag{1}$$

with $r_f$ being the Fresnel reflection coefficient, $\alpha_{eff}$ the effective polarizability, $E_0$ the incident field, $s$ the amplitude of the scattered field and $e^{i\alpha}$ the phase factor of the scattered field.[4,5] However, the local near-field $E_{loc}$ imaged in s-SNOM experiments is a convolution of the incident laser's far field ($E_0$) and the field of the localized surface plasmons $E_{LSP}$ such that $E_{loc} \propto E_{LSP} + E_0$.[2] At resonance the local near-field is dominant over the background signal $E_0$ ($E_0 \ll E_{LSP}$), such that $E_{loc} \approx E_{LSP}$.[2] Hence polarizing for P-detection selects the z-component of the scattered field, further eliminating contributions from dominant modes longitudinal to the probe shaft, and hence tip-sample interactions and $E_0$ from the s-SNOM technique.[1,2] The extracted near-field amplitude signal ($s_n$) and phase ($\phi_n$)sent to the detector signal is demodulated at a higher harmonic n$\Omega$ (n=2, 3, 4) of the tip vibration frequency $\Omega$ to suppress background contributions. As a result we have observed that in using S/P scheme imaging with a metallic tip Au and Si give similar results. However unlike S/P technique, in S/S excitation/detection scheme in strong plasmon coupling imaging, the role of the probe tip becomes critical and can significantly influence the resulting local near-field distribution[6–8] by changing the dielectric value of the gap to inductive/capacitive, as we have recently demonstrated.[9]

In triangular plasmonic antennas, the higher amplitude signal at the sharp triangle tip than at the base is a combination of strong field concentration at the tip and shift of resonance frequency as the base widens.[10,11] In Fig. 1 this is illustrated by FDTD calculation of the intensity at the sharp end of triangular structures as the wavelength is varied from 9-13 $\mu$m, for different base widths. The symmetric rod (50 nm base and tip) has a sharper resonance peak at 10.5 $\mu$m than any other geometry. The peak intensity diminishes and the linewidth broadens as the base is widened. The resonance peak begins to shift at about 600 nm base width. At 1500 nm, the intensity attains a weak maximum at 10.9 $\mu$m. We note that the contribution of dipolar resonance shift is a small effect at the experimental base width value of 450 nm.

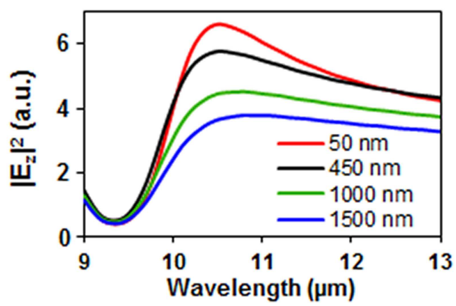


FIG. 1. FDTD mid-infrared spectroscopic ($\lambda$=9-13 $\mu$m) calculation of the intensity at the sharp end of Au plasmonic antennas for varying base widths (see legend). The sharp end has a fixed width of 50 nm, with fixed particle length of 1800 nm.

Furthermore, increasing the width of the base shifts the localization of the strong near-fields at the ends of the triangle as shown in Fig. 2. In analogy with the definition of the "hotspot," which is the field intensity maximum on the particle,[1,2,9,12–14] we define the "darkspot" as the field intensity minimum on the particle which also characterizes plasmon dipolar modes. As the base widens, the darkspot shifts towards the base end of the antenna due to a decrease in the overall charge density in the region. Thus the triangular plasmonic structures support asymmetric dipolar modes.[1,10,11,15,16] We also note that as the base width becomes larger than 600 nm, the resonance wavelength begins to red-shift as in Fig. 1. These results indicate the importance of geometry for hotspot localization and optimization of design for such plasmonic structures.

To further understand the role of triangular antenna length in the spectroscopic characteristics of the struc-

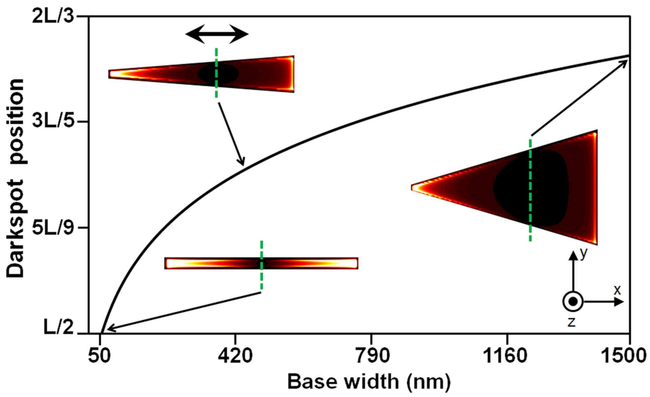


FIG. 2. Field intensity minimum ("darkspot") position relative to particle length (L=1800 nm) is plotted against base width (horizontal axis), FDTD simulation, $\lambda$=10.5 $\mu$m. Insets show intensity images calculated at the indicated base widths, with darkspot positions marked on the particle with the green vertical dotted line and excitation polarization direction relative to triangle antenna models marked with thick black arrow. Coordinate axes are defined at bottom right

.

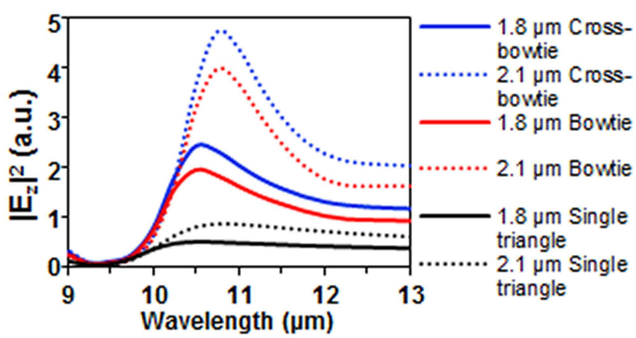


FIG. 3. Spectroscopic FDTD simulation near-field intensity at the sharp tip region of antenna structures comprised of either longer (2.1 $\mu$m) or shorter (1.8 $\mu$m) single triangle elements. The bowtie and cross-bowties have a gap size of 60 nm.

tures, we simulated the spectroscopic response of each structure using FDTD for lengths of 1.8 $\mu$m and 2.1 $\mu$m, in the range $\lambda$=9-13 $\mu$m wavelength as shown in Fig. 3. The gap width of the bowties is set at 60 nm in order to match the minimum gap possible in the cross-bowties, owing to the 50 nm sharp tip width. We again find that the intensity scales with increasing particle length,[3,10,12,17–23] with an intensity in cross-bowties ∼20-30% greater than bowties, and ∼200-450% greater than single rod structures. The calculation also shows a redshift of the broad resonance peaks (∼2 $\mu$m at FWHM) as particle length is increased for a fixed gap width >10 nm.

Figure 4 shows FDTD simulation of the spectroscopy of fixed-length (1800 nm) bowties with gaps ranging from 5 nm-170 nm, including comparisons to a cross-bowtie

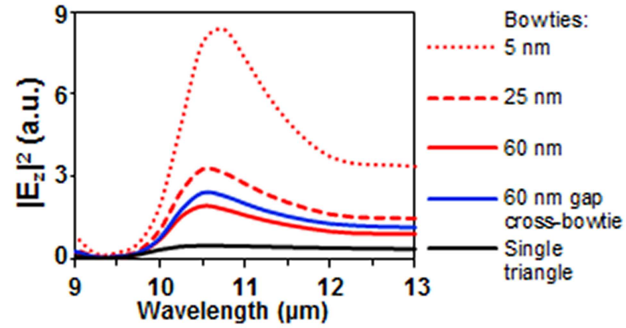


FIG. 4. Spectroscopic FDTD simulation results for near-field intensity calculated at the sharp tips of bowties for three gap widths (red curves), a 60 nm gap cross-bowtie and a single triangle.

with 60 nm gap, and a single triangle for reference. Except for the 5 nm bowtie, all structures comprised of a fixed antenna length display a resonance peak at $\lambda \approx$10.5 $\mu$m. We note that only gap widths <10 nm produce a redshift in resonance, as demonstrated by a ∼250 nm resonance redshift to ∼10.75 $\mu$m wavelength in the 5 nm bowtie.[24–27] We also note that the total near-field intensity increases as the fields are confined in smaller gaps.[3,9] Finally, the single triangle forms a limiting case for infinitely large gaps, and the reduction in intensity asymptotically approaches this value as gap width is increased.

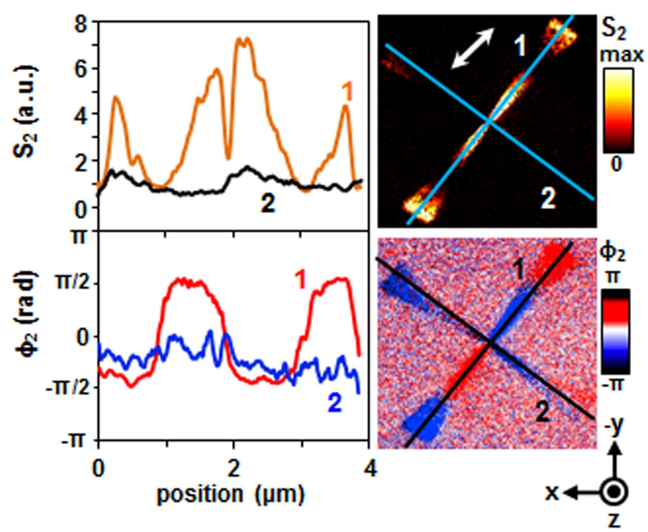


FIG. 5. Left shows mid-infrared ($\lambda$=10.5 $\mu$m) s-SNOM optical near-field amplitude $s_2$ and phase $\phi_2$ line profiles based on the lines labeled at right of the bowties parallel to (1) and perpendicular to (2) the excitation laser polarization direction (white arrow) and coordinate axes defined at bottom right.

In Fig. 5, we examine the effect of excitation laser polarization on a cross-bowtie with s-SNOM experimental optical images. Figure 5 shows amplitude $s_2$ and phase $\phi_2$ line profiles taken from the correspondingly labeled lines (1) and (2) in the s-SNOM images (Fig. 5). In these images the incident laser polarization direction is parallel to lines (1), and consequently perpendicular to lines (2). We see that the polarization-parallel arms of line (1) in Fig. 5 display strong optical contrast at the sharp tips of the triangles compared to the wider base ends. The position of the darkspot on each arm occurs closer to the base ends than the sharp tip ends. The phase line profiles (1) in Fig. 5 also show marked contrast in each corresponding blue and red region, indicating strong dipolar coupling between these elements.[1,2] Since the cross-bowtie is symmetric with respect to a 90° rotation, lines (2) illustrate the behavior of a bowtie aligned perpendicular to the laser polarization. The amplitude contrast is weak, with some variation near the 0 $\mu$m and 2 $\mu$m tick marks due to minor misalignment of the sample with the excitation polarization.[3] The phase line profile (2) in Fig. 5 appears noisy along the center, along the splitting point of the phase. This is observed visually in the image $\phi_2$ of Fig. 5, where the phase changes from ∼-90° to ∼90° across the short axis of the antenna.

To explore the effect of sample rotation with respect to a fixed polarization of the light source, we simulated the evolution of the near-field intensity images of a cross-bowtie, shown in Fig. 6. At 90°, the arms marked B are aligned with the polarization direction of the incident excitation source and display clear dipolar modes,[1,2] and the arms labeled A are perpendicular to the light polarization, and have weak intensity at the edges. As the structure is rotated, the dipolar modes of B fade as the arms leave alignment, while the A arms are increasingly resonant as they rotate into alignment with the applied field.[3,28] The line profiles for the A and B arms clearly show the localized field evolution over a 90° rotation with respect to a horizontally-oriented excitation.

* Yohannes.Abate@csulb.edu


1 D.-S. Kim and Z. H. Kim, *Opt. Express*, 2012, **20**, 8689–8699.
2 D.-S. Kim, J. Heo, S.-H. Ahn, S. W. Han, W. S. Yun and Z. H. Kim, *Nano Lett.*, 2009, **9**, 3619–3625.
3 P. Alonso-González, P. Albella, F. Golmar, L. Arzubiaga, F. Casanova, L. E. Hueso, J. Aizpurua and R. Hillenbrand, *Opt. Express*, 2013, **21**, 1270–1280.
4 F. Huth, A. Govyadinov, S. Amarie, W. Nuansing, F. Keilmann and R. Hillenbrand, *Nano Lett.*, 2012, **12**, 3973–3978.
5 J. M. Stiegler, Y. Abate, A. Cvitkovic, Y. E. Romanyuk, A. J. Huber, S. R. Leone and R. Hillenbrand, *ACS Nano*, 2011, **5**, 6494–6499.
6 A. García-Etxarri, I. Romero, F. J. García de Abajo, R. Hillenbrand and J. Aizpurua, *Phys. Rev. B*, 2009, **79**, 125439.
7 A. Alù and N. Engheta, *Nature Photon.*, 2008, **2**, 307–310.
8 M. Schnell, A. García-Etxarri, A. J. Huber, K. Crozier, J. Aizpurua and R. Hillenbrand, *Nature Photon.*, 2009, **3**, 287–291.
9 S. Mastel, S. E. Grefe, G. B. Cross, A. Taber, S. Dhuey, S. Cabrini, P. J. Schuck and Y. Abate, *Appl. Phys. Lett.*, 2012, **101**, 131102.
10 H. Fischer and O. J. F. Martin, *Opt. Express*, 2008, **16**, 9144–9154.
11 Y.-Y. Yang, Y.-L. Zhang, F. Jin, X.-Z. Dong, X.-M. Duan and Z.-S. Zhao, *Opt. Commun.*, 2011, **284**, 3474 – 3478.
12 P. Alonso-González, P. Albella, M. Schnell, J. Chen, F. Huth, A. García-Etxarri, F. Casanova, F. Golmar, L. Arzubiaga, L. Hueso, J. Aizpurua and R. Hillenbrand, *Nat. Commun.*, 2012, **3**, 1–7.
13 M. Schnell, A. Garcia-Etxarri, J. Alkorta, J. Aizpurua and R. Hillenbrand, *Nano Lett.*, 2010, **10**, 3524–3528.
14 M. Schnell, P. Alonso-González, L. Arzubiaga, F. Casanova, L. E. Hueso, A. Chuvilin and R. Hillenbrand, *Nature Photon.*, 2011, **5**, 283–287.
15 P. Biagioni, M. Savoini, J. Huang, L. Duó, M. Finazzi and B. Hecht, *Phys. Rev. B*, 2009, **80**, 153409.
16 N. Yu, E. Cubukcu, L. Diehl, D. Bour, S. Corzine, J. Zhu, G. Höfler, K. B. Crozier and F. Capasso, *Opt. Express*, 2007, **15**, 13272.
17 L. Novotny, *Phys. Rev. Lett.*, 2007, **98**, 266802.
18 P. K. Jain, W. Huang and M. A. El-Sayed, *Nano Lett.*, 2007, **7**, 2080–2088.
19 A. M. Funston, C. Novo, T. J. Davis and P. Mulvaney, *Nano Lett.*, 2009, **9**, 1651–1658.
20 R. L. Olmon, P. M. Krenz, A. C. Jones, G. D. Boreman and M. B. Raschke, *Opt. Express*, 2008, **16**, 20295–20305.
21 P. Bharadwaj, B. Deutsch and L. Novotny, *Adv. Opt. Photon.*, 2009, **1**, 438–483.
22 S. Eustis and M. A. El-Sayed, *Chem. Soc. Rev.*, 2006, **35**, 209–217.
23 L. Novotny and N. van Hulst, *Nature Photon.*, 2011, **5**, 83–90.
24 J.-S. Huang, J. Kern, P. Geisler, P. Weinmann, M. Kamp, A. Forchel, P. Biagioni and B. Hecht, *Nano Lett.*, 2010, **10**, 2105–2110.
25 S. Pillai, K. R. Catchpole, T. Trupke, G. Zhang, J. Zhao and M. A. Green, *Appl. Phys. Lett.*, 2006, **88**, 161102.
26 K.-H. Su, Q.-H. Wei, X. Zhang, J. J. Mock, D. R. Smith and S. Schultz, *Nano Lett.*, 2003, **3**, 1087–1090.
27 J. A. Fan, C. Wu, K. Bao, B. J. Kui, R. Bardhan, N. J. Halas, V. N. Manoharan, P. Nordlander, G. Shvets and F. Capasso, *Science*, 2010, **328**, 1135–1138.
28 T. Ellenbogen, K. Seo and K. B. Crozier, *Nano Lett.*, 2012, **12**, 1026–1031.

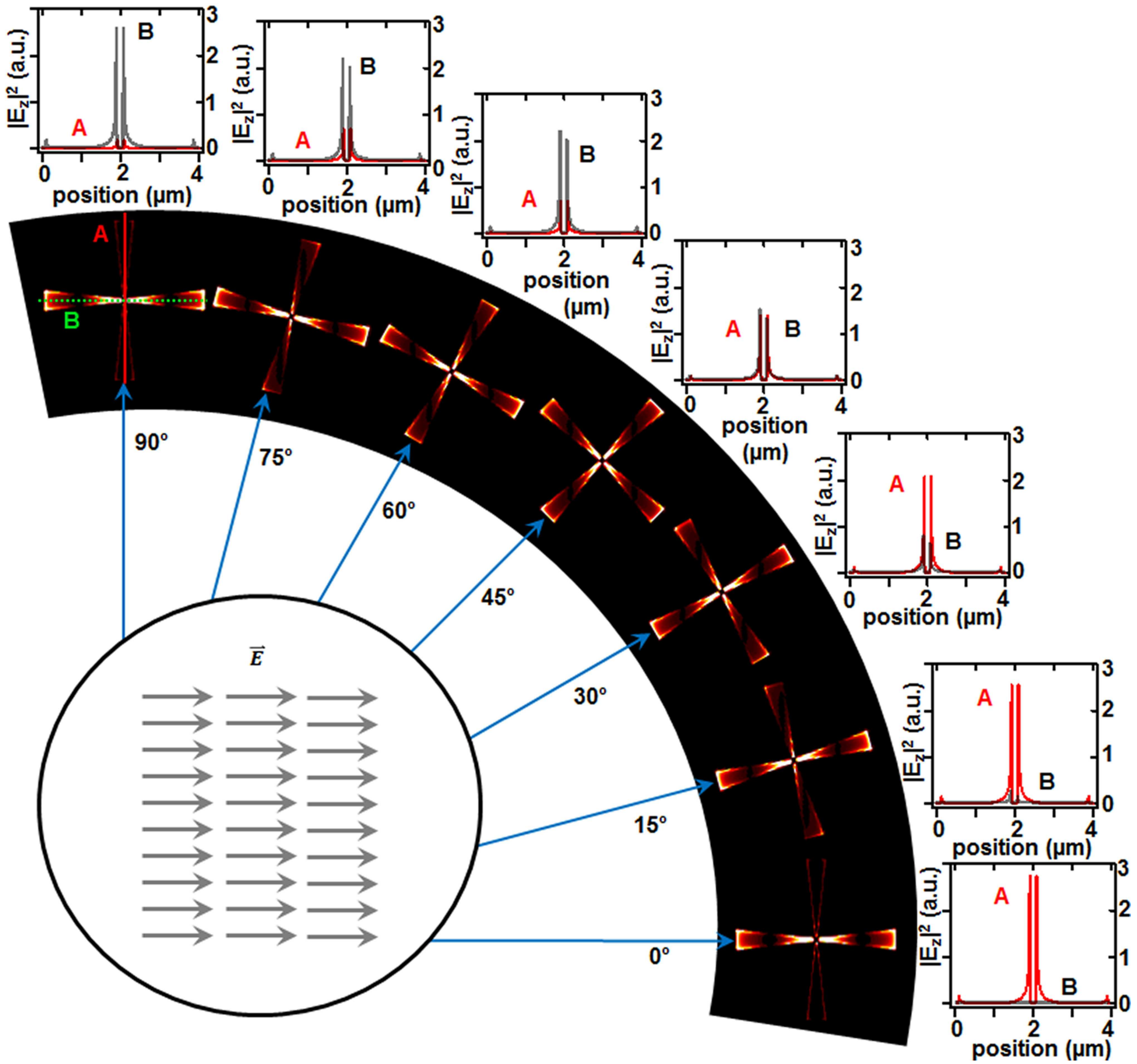


FIG. 6. Near-field intensity images of cross-bowtie antennas, simulated by FDTD method at light source excitation wavelength $\lambda$=10.5 $\mu$m and excitation polarization direction marked by gray arrows. The lines marked A and B in the 90° intensity image are plotted as line profiles in each corresponding graph.